

Supplementary Information:

Simultaneously enhancing power factor and reducing thermal conductivity of SnTe via introducing its analogues

Xiao Zhang,^{a,†} Dongyang Wang,^{a,†} Haijun Wu,^{b,†} Meijie Yin,^{c,d} Yanling Pei,^a Shengkai Gong,^a Li Huang,^{c,d} Stephen John Pennycook,^b Jiaqing He^{c,d} and Li-Dong Zhao^{a,*}

^aSchool of Materials Science and Engineering, Beihang University, Beijing 100191, China

^bDepartment of Materials Science and Engineering, National University of Singapore, 7 Engineering Drive 1, Singapore 117575, Singapore

^cDepartment of Physics, Southern University of Science and Technology, Shenzhen 518055, China

^dShenzhen Key Laboratory of Thermoelectric Materials, Shenzhen 518055, China

†These authors contributed equally to this work

*Corresponding author: zhaolidong@buaa.edu.cn

EXPERIMENTAL

Starting materials: Reagent chemicals were used as obtained: Sn chunk (99.999%), Te shot (99.999%, Aladdin, China), Bi shot (99.999%, Aladdin, China), S chunk (99.99%, Aladdin, China), Pb shot (99.999%, Aladdin, China), and Se shot (99.999%, Aladdin, China).

Synthesis: High-purity single elements Sn, Ga, In, Bi, Sb, Sr, and Te were weighed according to the nominal compositions of $\text{Sn}_{0.97}\text{Bi}_{0.03}\text{Te}$ with $x\%$ PbTe/PbSe/PbS/SnSe/SnS (mol fraction in the text, $x = 0, 1, 2, 3, 4$ and 5). And put them inside the 13-mm-diameter fused quartz tubes. The tubes were sealed under vacuum ($\sim 10^{-4}$ Torr) and slowly heated to 723 K in 12 h and then to 1423 K in 6 h, soaked at this temperature for 6 h, and subsequently cooled in a furnace to room temperature. The resultant ingots were crushed into fine powders by hand milling and then densified by a spark plasma sintering (SPS) method (SPS-211LX, Fuji Electronic Industrial Co., Ltd.) at 923 K for 3 min in a 15 mm diameter graphite die under an axial compressive stress of 40 MPa in vacuum. Highly dense ($>95\%$ of theoretical density, Table S1) disk-shaped pellets with dimensions of 15 mm in diameter and 6 mm in thickness were obtained.

Phase and microstructures: The phase structure was characterized by X-ray diffraction (XRD) using a D/max 2500PC diffractometer with $\text{Cu K}\alpha$ ($\lambda = 1.5418 \text{ \AA}$) radiation in a reflection geometry on an Inel diffractometer operating at 40 kV and 20 mA and equipped with a position-sensitive detector. (Scanning)/transmission electron microscopy (STEM and TEM) and energy dispersive X-ray spectroscopy (EDS) studies were conducted using a JEOL ARM200F atomic resolution analytical electron microscope installed in the National University of Singapore equipped with a cold field-emission gun, a new ASCOR 5th order aberration corrector and Gatan OneView camera and an Oxford X-Max 100TLE X-ray detector. Some TEM observations were performed under 300 KV for the microstructure on the FEI Tecnai F30.

Electrical transport properties: The obtained pellets were cut into bars with dimensions $14 \times 3 \times 3 \text{ mm}^3$ which were used for the simultaneous measurement of the Seebeck coefficient and the electrical conductivity using an Ulvac Riko ZEM-3 instrument under a low-pressure

helium atmosphere at 300-900K. The samples were coated with a thin ($\sim 0.1-0.2$ mm) layer of boron nitride (BN) to protect the instruments. The uncertainty of the Seebeck coefficient and electrical conductivity measurements is 3%. Hall coefficient (R_H) is measured under a reversible magnetic field (0.8 T) by the Van der Pauw method by using a Hall measurement system (Lake Shore 8400 Series, Model 8404, USA). Carrier density (n_H) is obtained by $n_H = 1/(e \cdot R_H)$, and carrier mobility (μ_H) is calculated using the relationship $\mu_H = \sigma \cdot R_H$ with σ being the electrical conductivity obtained from ZEM-3 instrument.

Thermal transport properties: The obtained pellets were cut into thin wafer with dimensions $\Phi 6 \times 2$ mm³ for thermal diffusivity measurements using a laser flash diffusivity method in a Netzsch LFA457. The samples were coated with a thin layer of graphite to minimize errors from the material emissivity. The thermal conductivity was calculated as $\kappa = D \cdot Cp \cdot \rho$, where D is the thermal diffusivity coefficient, Cp is the specific heat capacity indirectly derived using a reference sample (Pyroceram 9606), and the density (ρ) was determined using the dimensions and mass of the sample. The uncertainty of the thermal conductivity is estimated to be within 10%, comprising uncertainties of 3% for the thermal diffusivity (D), 5% for the specific heat (Cp), and 2% for the sample density (d). The combined uncertainty for all measurements involved in the calculation of ZT is around 20%.

Band structure calculations: First-principles calculations within density functional theory (DFT) have been performed for $\text{Sn}_{0.97}\text{Bi}_{0.03}\text{Te}-3\% \text{ M}$ ($\text{M} = \text{PbTe}, \text{PbSe}, \text{PbS}, \text{SnSe}, \text{and SnS}$) using the projector-augmented wave (PAW) method^{1, 2} as implemented in the Vienna Ab-initio Simulation Package (VASP)³. The exchange-correlation energy is treated in the generalized gradient approximation (GGA) Perdew-Burke-Ernzerhof (PBE)⁴. Since the atoms in these compounds are heavy elements, the effects of spin-orbit coupling (SOC) are included in our calculations. Plane waves with an energy cutoff of 450 eV are used as the basis set for all the systems. Defects in SnTe are modeled using a $2 \times 2 \times 2$ supercell consisting of 64 atoms modified with one Bi substituted Sn site (Bi_{Sn}), and one Pb(S) substituted Sn(Te) site ($\text{Pb}_{\text{Sn}}/\text{S}_{\text{Te}}$). A Monkhorst-Pack Γ -centered $6 \times 6 \times 6$ k-point mesh is used for Brillouin zone sampling. All the structures are fully relaxed until the maximum residual ionic force is below 0.02 eV/Å, and the total energy difference is converged to within 10^{-6} eV. Multiple

configurations can form with different relative positions between substituted Sn and Te sites. We calculate the electronic structures of four configurations for $\text{Sn}_{0.97}\text{Bi}_{0.03}\text{Te}$ -3% PbSe system, and find that different configurations essentially have the same band structures, as shown in Figure S15.

REFERENCES

1. P. E. Blöchl, *Physical Review B*, 1994, **50**, 17953.
2. G. Kresse and D. Joubert, *Physical Review B*, 1999, **59**, 1758.
3. G. Kresse and J. Furthmüller, *Physical Review B*, 1996, **54**, 11169.
4. J. P. Perdew, K. Burke and M. Ernzerhof, *Physical Review Letters*, 1996, **77**, 3865.

Table S1. Sample densities included in the study.

Samples	Theoretical Density, [g/cc]	Measured Density, [g/cc]	[%] Density	Theoretical
Sn _{0.97} Bi _{0.03} Te	6.445	6.398	99.27	
Sn _{0.97} Bi _{0.03} Te-1% PbTe	6.46219	6.301	97.51	
Sn _{0.97} Bi _{0.03} Te-2% PbTe	6.47938	6.303	97.28	
Sn _{0.97} Bi _{0.03} Te-3% PbTe	6.49657	6.31	97.13	
Sn _{0.97} Bi _{0.03} Te-4% PbTe	6.51376	6.312	96.90	
Sn _{0.97} Bi _{0.03} Te-5% PbTe	6.53095	6.311	96.63	
Sn _{0.97} Bi _{0.03} Te-1% PbSe	6.46313	6.298	97.44	
Sn _{0.97} Bi _{0.03} Te-2% PbSe	6.48126	6.3	97.20	
Sn _{0.97} Bi _{0.03} Te-3% PbSe	6.49939	6.23	95.86	
Sn _{0.97} Bi _{0.03} Te-4% PbSe	6.51752	6.305	96.75	
Sn _{0.97} Bi _{0.03} Te-5% PbSe	6.53565	6.308	96.52	
Sn _{0.97} Bi _{0.03} Te-1% PbS	6.45634	6.297	97.53	
Sn _{0.97} Bi _{0.03} Te-2% PbS	6.46768	6.302	97.44	
Sn _{0.97} Bi _{0.03} Te-3% PbS	6.47902	6.4706	99.87	
Sn _{0.97} Bi _{0.03} Te-4% PbS	6.49036	6.309	97.21	
Sn _{0.97} Bi _{0.03} Te-5% PbS	6.5017	6.282	96.62	
Sn _{0.97} Bi _{0.03} Te-1% SnSe	6.44234	6.3	97.79	
Sn _{0.97} Bi _{0.03} Te-2% SnSe	6.43968	6.298	97.80	
Sn _{0.97} Bi _{0.03} Te-3% SnSe	6.43702	6.297	97.82	
Sn _{0.97} Bi _{0.03} Te-4% SnSe	6.43436	6.295	97.83	
Sn _{0.97} Bi _{0.03} Te-5% SnSe	6.4317	6.296	97.89	
Sn _{0.97} Bi _{0.03} Te-1% SnS	6.43135	6.299	97.94	
Sn _{0.97} Bi _{0.03} Te-2% SnS	6.4177	6.297	98.12	
Sn _{0.97} Bi _{0.03} Te-3% SnS	6.40405	6.298	98.34	
Sn _{0.97} Bi _{0.03} Te-4% SnS	6.3904	6.296	98.52	
Sn _{0.97} Bi _{0.03} Te-5% SnS	6.37675	6.294	98.70	

Using the densities of SnTe of 6.445 g/cc, PbTe of 8.164, PbSe of 8.258 g/cc, PbS of 7.579 g/cc, SnSe of 6.179 g/cc and SnS of 5.08 g/cc, the theoretical density $\rho(x)$ of the SnTe-y at.% PbTe / PbSe / PbS / SnSe / SnS ($y = 0, 1, 2, 3, 4, 5$) samples were calculated using:

$$\rho(x) = (1-x)\rho_{\text{SnTe}} + (x)\rho_{\text{PbTe / PbSe / PbS / SnSe / SnS}}$$

where x is volume fraction.

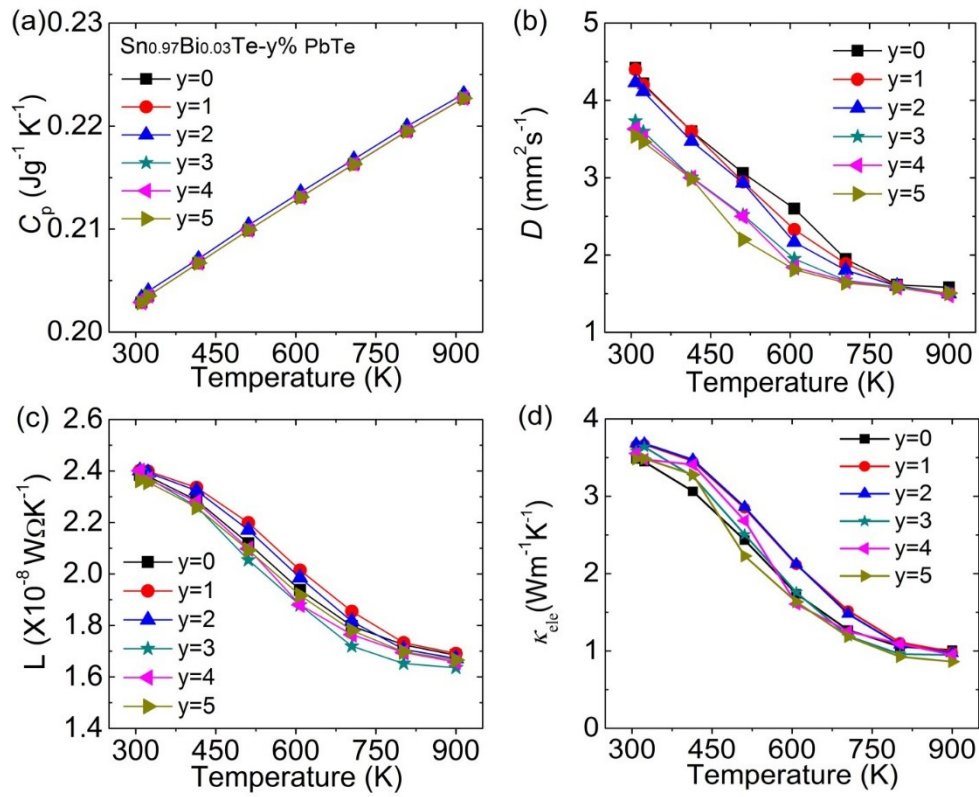


Figure S1. Thermoelectric properties as a function of temperature for $\text{Sn}_{0.97}\text{Bi}_{0.03}\text{Te}-y\% \text{PbTe}$ ($y = 0, 1, 2, 3, 4$ and 5): (a) heat capacity; (b) thermal diffusivity; (c) Lorenz number; (d) electronic thermal conductivity.

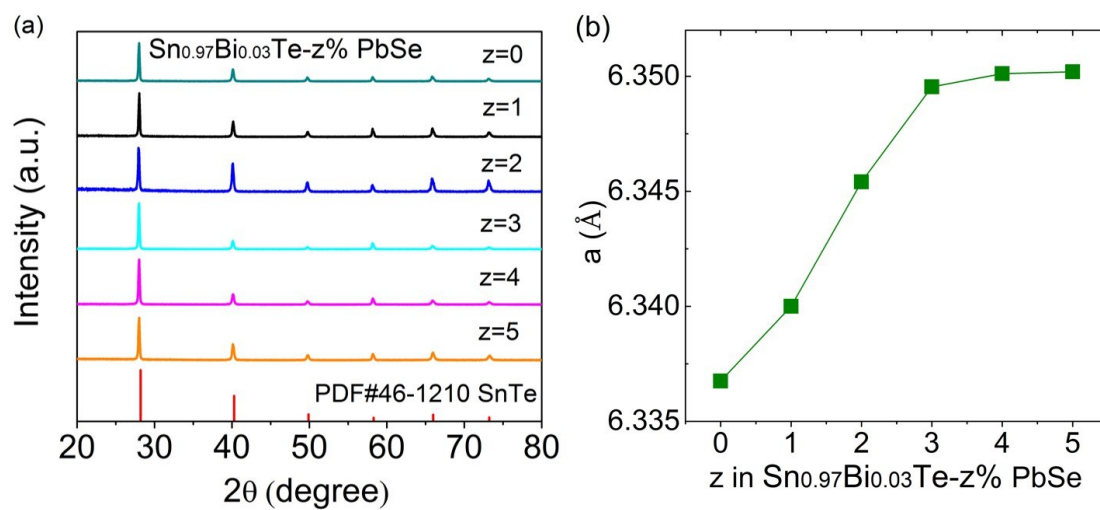


Figure S2. (a) Powder XRD patterns of $\text{Sn}_{0.97}\text{Bi}_{0.03}\text{Te}-z\% \text{PbSe}$ ($z = 0, 1, 2, 3, 4$ and 5); (b) lattice parameter as a function of PbSe fractions.

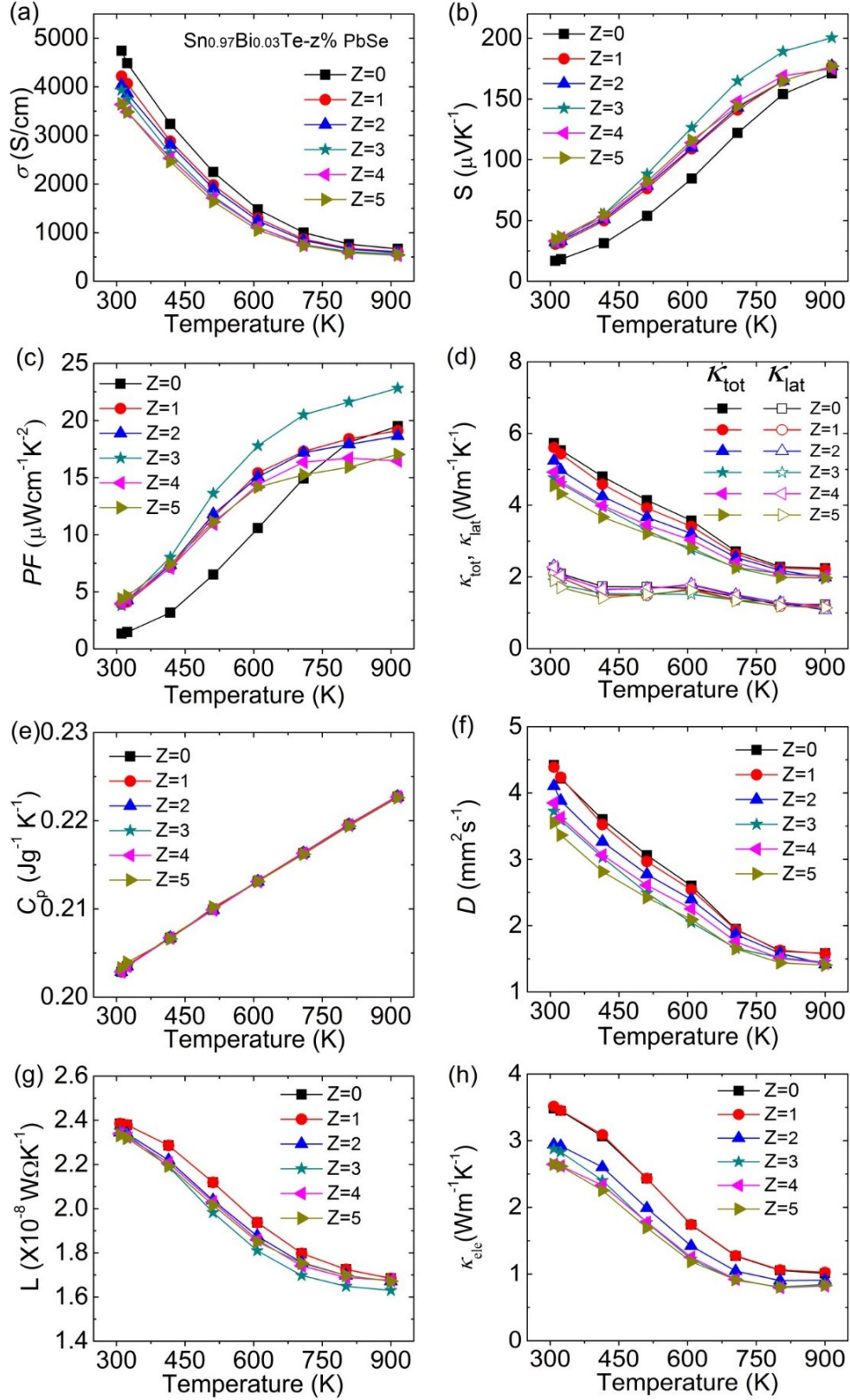


Figure S3. Thermoelectric properties as a function of temperature for $\text{Sn}_{0.97}\text{Bi}_{0.03}\text{Te}-z\% \text{PbSe}$ ($z = 0, 1, 2, 3, 4$ and 5): (a) electrical conductivity; (b) Seebeck coefficient; (c) power factor; (d) total and lattice thermal conductivities; (e) heat capacity; (f) thermal diffusivity; (g) Lorenz number; (h) electronic thermal conductivity.

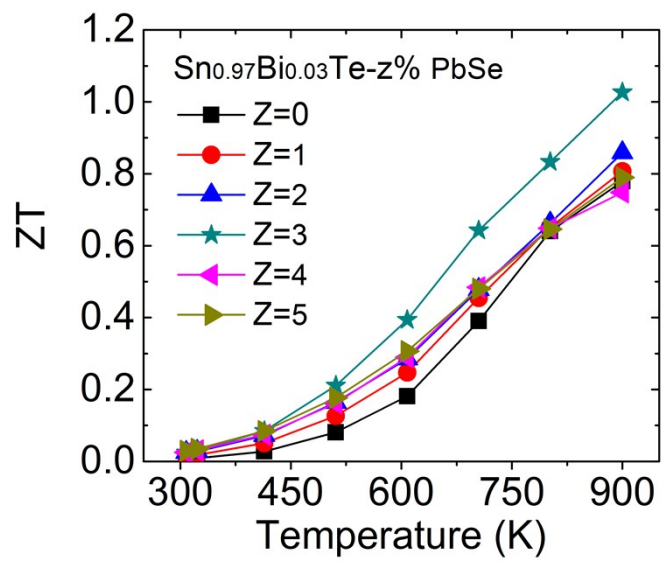


Figure S4. ZT values as a function of temperature for $\text{Sn}_{0.97}\text{Bi}_{0.03}\text{Te}-z\% \text{PbSe}$ ($z = 0, 1, 2, 3, 4$ and 5).

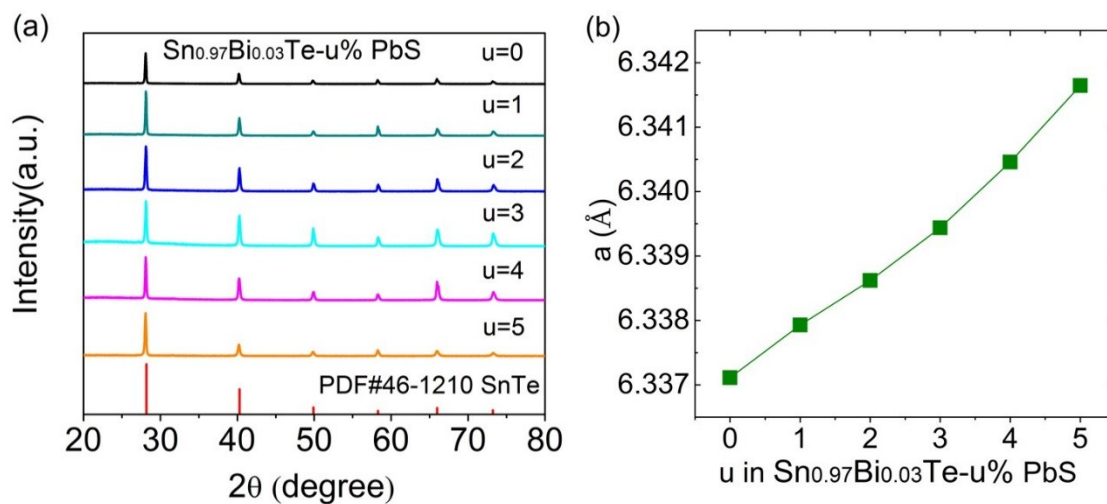


Figure S5. (a) Powder XRD patterns of $\text{Sn}_{0.97}\text{Bi}_{0.03}\text{Te}-u\% \text{PbS}$ ($u = 0, 1, 2, 3, 4$ and 5); (b) lattice parameter as a function of PbS fractions.

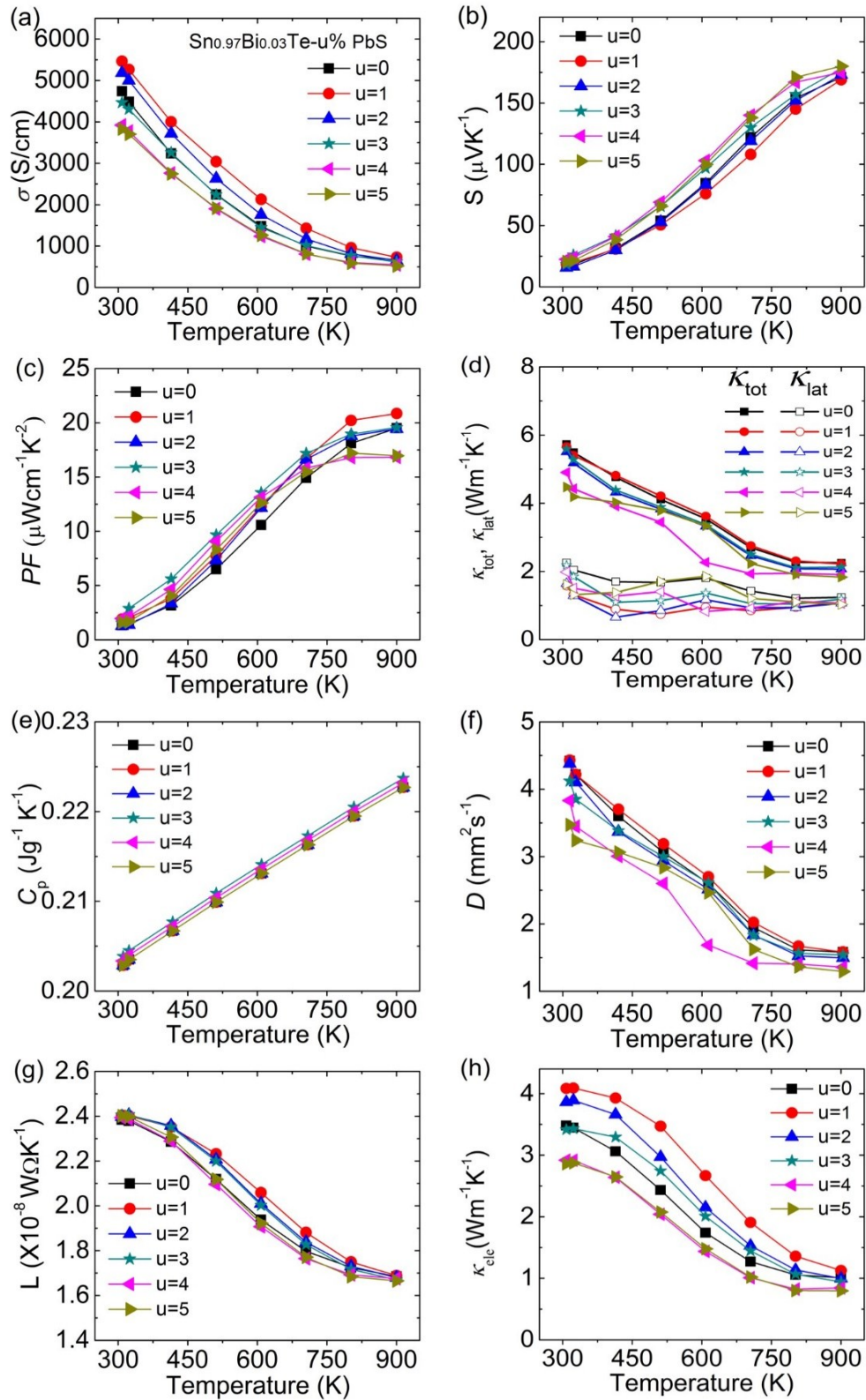


Figure S6. Thermoelectric properties as a function of temperature for $\text{Sn}_{0.97}\text{Bi}_{0.03}\text{Te}-u\% \text{PbS}$ ($u = 0, 1, 2, 3, 4$ and 5): (a) electrical conductivity; (b) Seebeck coefficient; (c) power factor; (d) total and lattice thermal conductivities; (e) heat capacity; (f) thermal diffusivity; (g) Lorenz number; (h) electronic thermal conductivity.

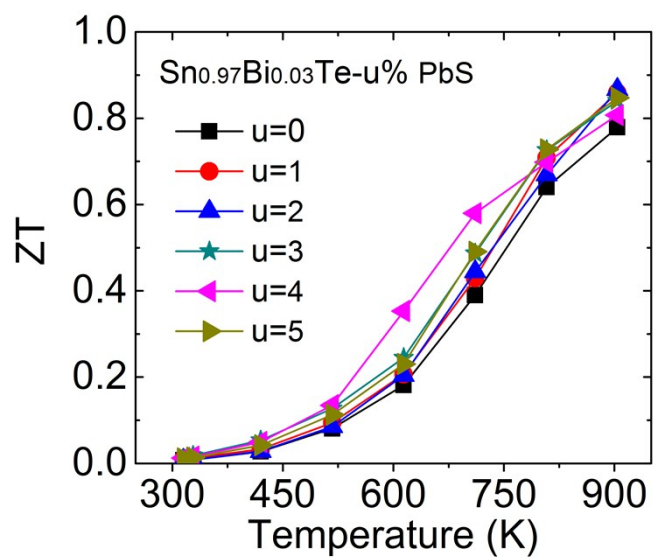


Figure S7. ZT values as a function of temperature for $\text{Sn}_{0.97}\text{Bi}_{0.03}\text{Te}-u\% \text{PbS}$ ($u = 0, 1, 2, 3, 4$ and 5).

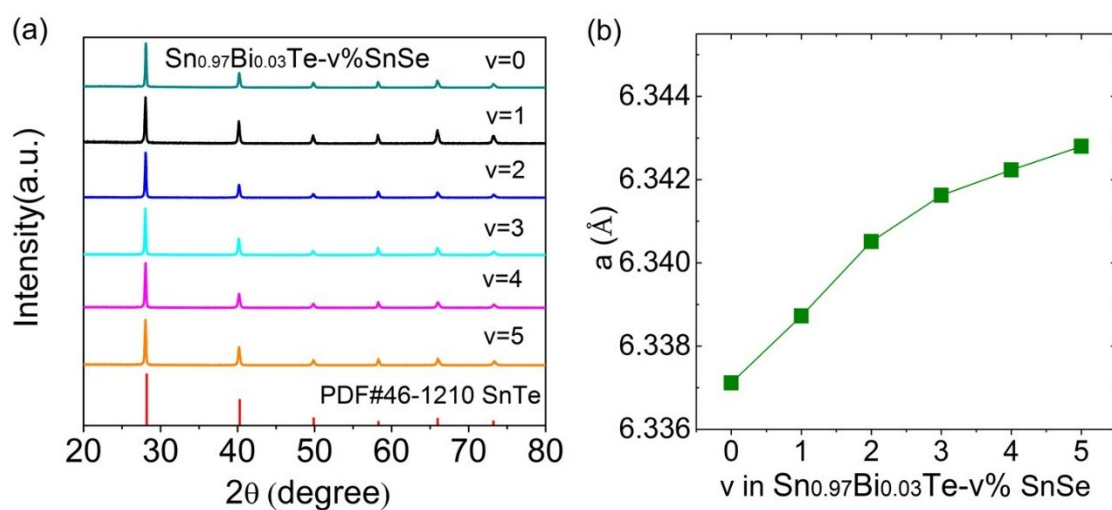


Figure S8. (a) Powder XRD patterns of $\text{Sn}_{0.97}\text{Bi}_{0.03}\text{Te}-v\% \text{SnSe}$ ($v = 0, 1, 2, 3, 4$ and 5); (b) lattice parameter as a function of SnSe fractions.

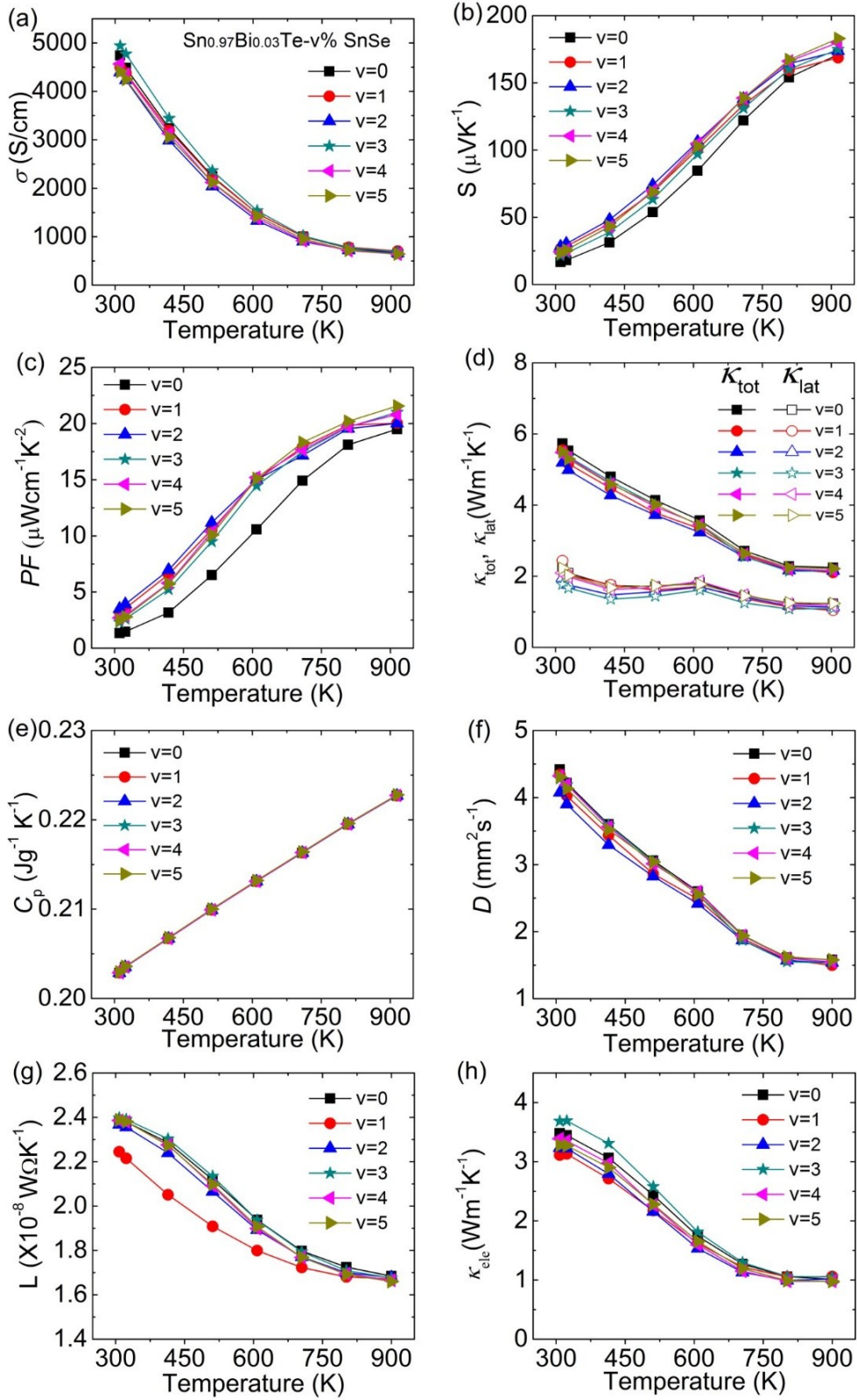


Figure S9. Thermoelectric properties as a function of temperature for $\text{Sn}_{0.97}\text{Bi}_{0.03}\text{Te}-v\%$ SnSe ($v = 0, 1, 2, 3, 4$ and 5): (a) electrical conductivity; (b) Seebeck coefficient; (c) power factor; (d) total and lattice thermal conductivities; (e) heat capacity; (f) thermal diffusivity; (g) Lorenz number; (h) electronic thermal conductivity.

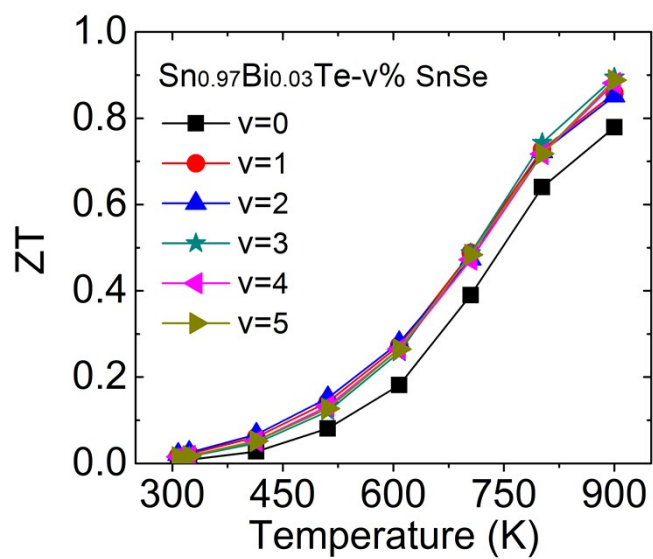


Figure S10. ZT values as a function of temperature for $\text{Sn}_{0.97}\text{Bi}_{0.03}\text{Te}-v\% \text{SnSe}$ ($v = 0, 1, 2, 3, 4$ and 5).

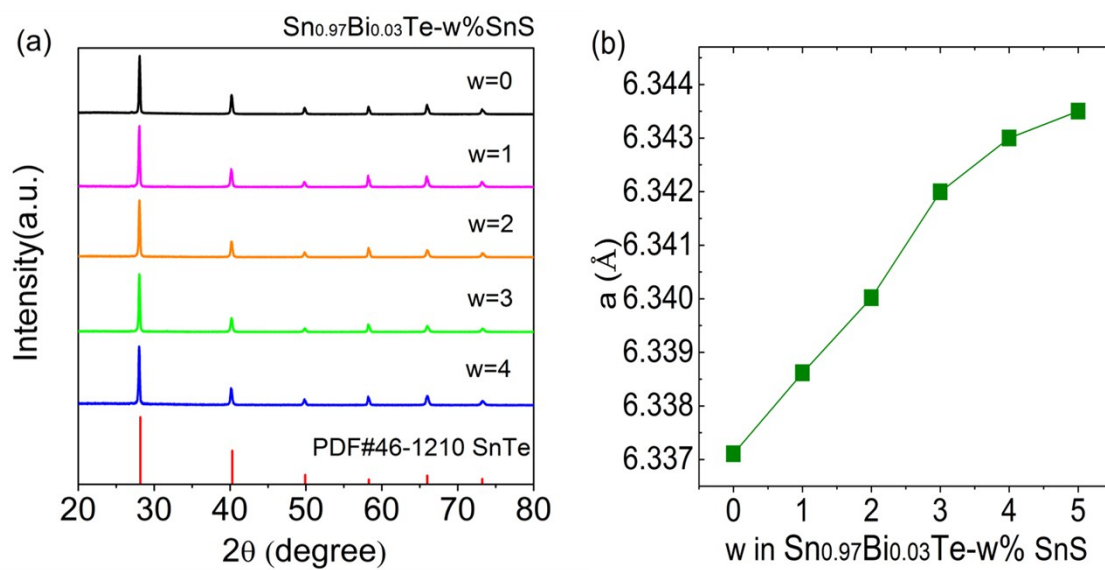


Figure S11. (a) Powder XRD patterns of $\text{Sn}_{0.97}\text{Bi}_{0.03}\text{Te}-w\% \text{SnS}$ ($w = 0, 1, 2, 3, 4$ and 5); (b) lattice parameter as a function of SnS fractions.

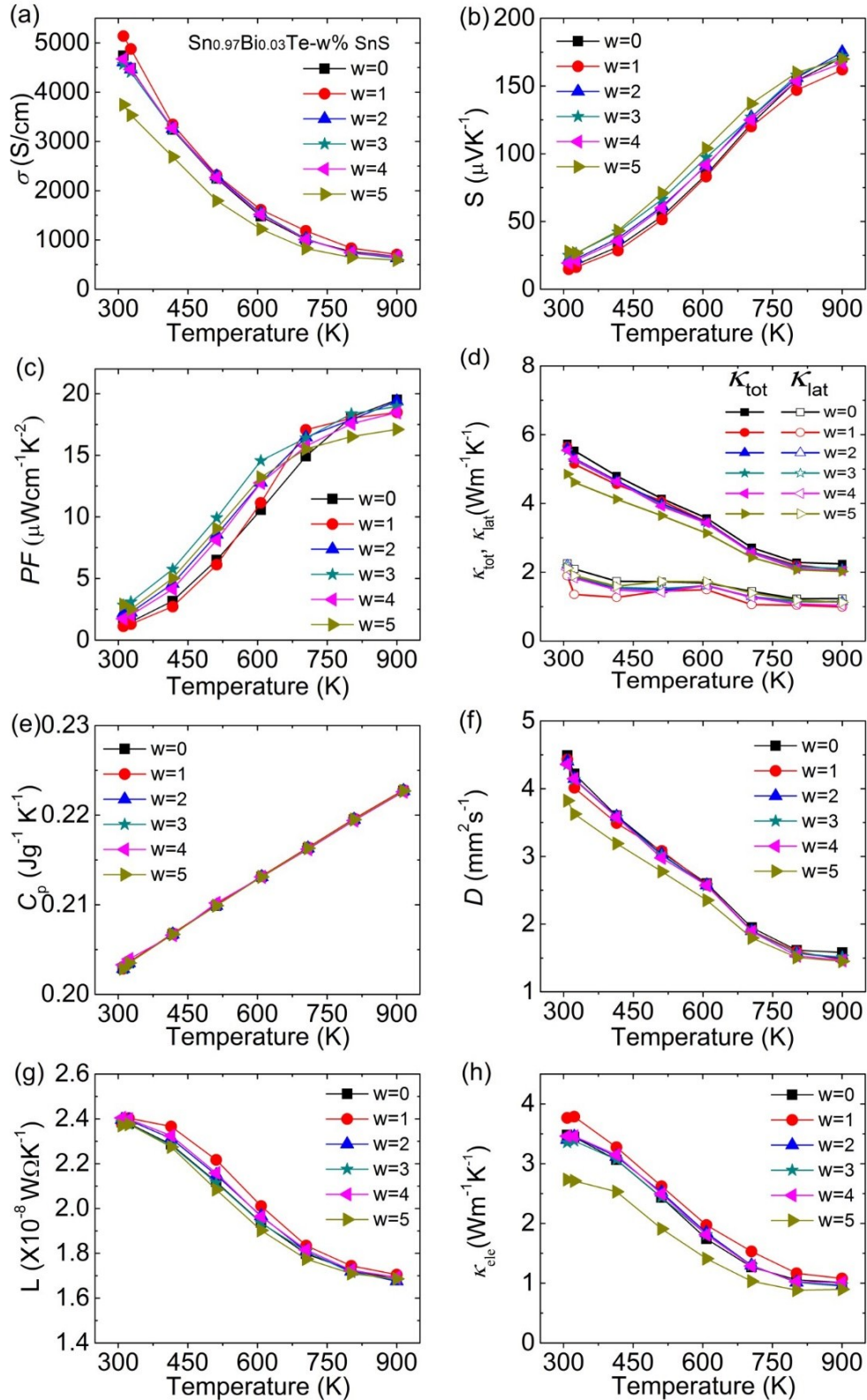


Figure S12. Thermoelectric properties as a function of temperature for $\text{Sn}_{0.97}\text{Bi}_{0.03}\text{Te}-w\% \text{SnS}$ ($w = 0, 1, 2, 3, 4$ and 5): (a) electrical conductivity; (b) Seebeck coefficient; (c) power factor; (d) total and lattice thermal conductivities; (e) heat capacity; (b) thermal diffusivity; (c) Lorenz number; (d) electronic thermal conductivity.

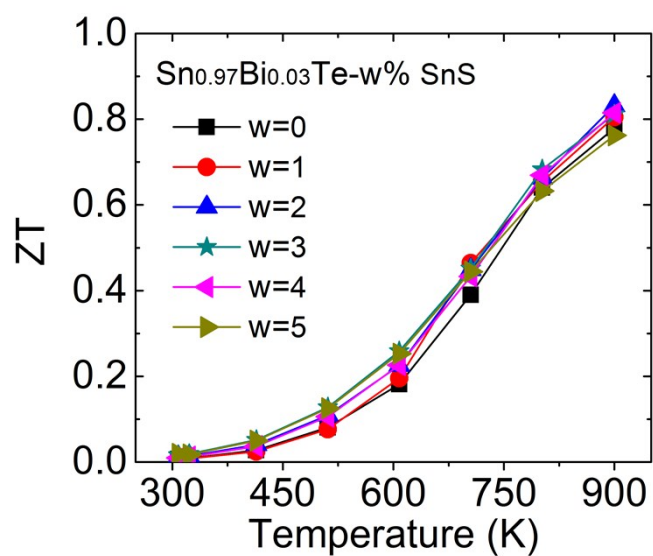


Figure S13. ZT values as a function of temperature for $\text{Sn}_{0.97}\text{Bi}_{0.03}\text{Te}-w\% \text{SnS}$ ($w = 0, 1, 2, 3, 4$ and 5).

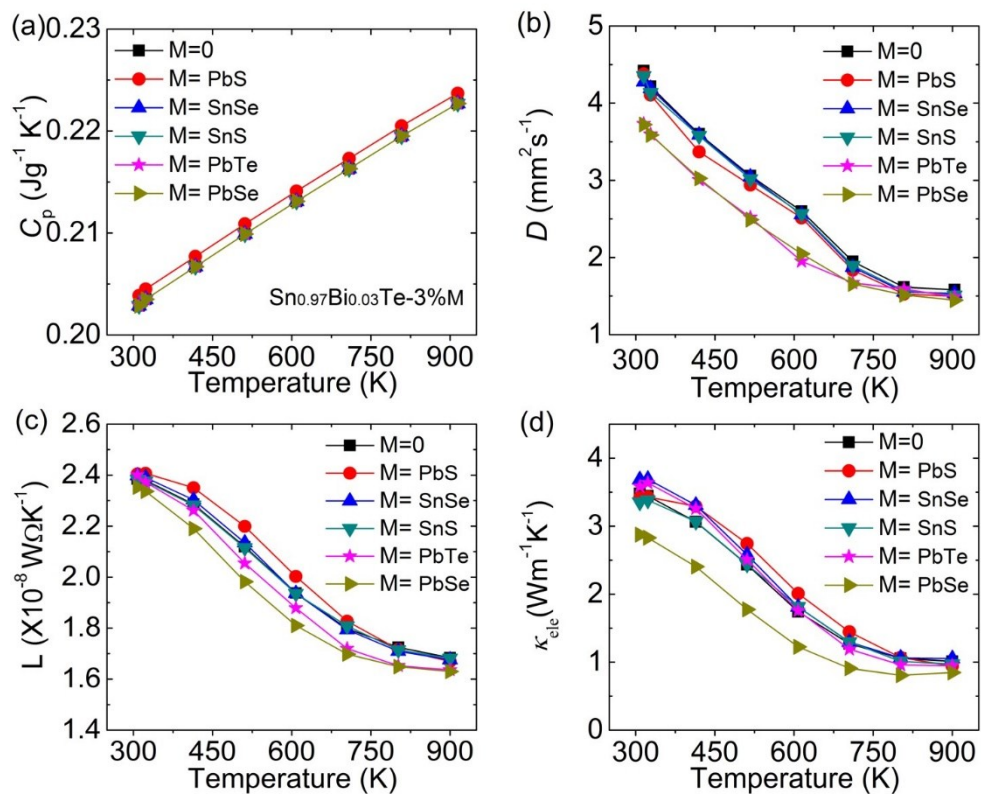


Figure S14. Thermoelectric properties as a function of temperature for $\text{Sn}_{0.97}\text{Bi}_{0.03}\text{Te}$ and $\text{Sn}_{0.97}\text{Bi}_{0.03}\text{Te}$ with 3.0% M (M = PbS, SnSe, SnS, PbTe, and PbSe): (a) heat capacity; (b) thermal diffusivity; (c) Lorenz number; (d) electronic thermal conductivity.

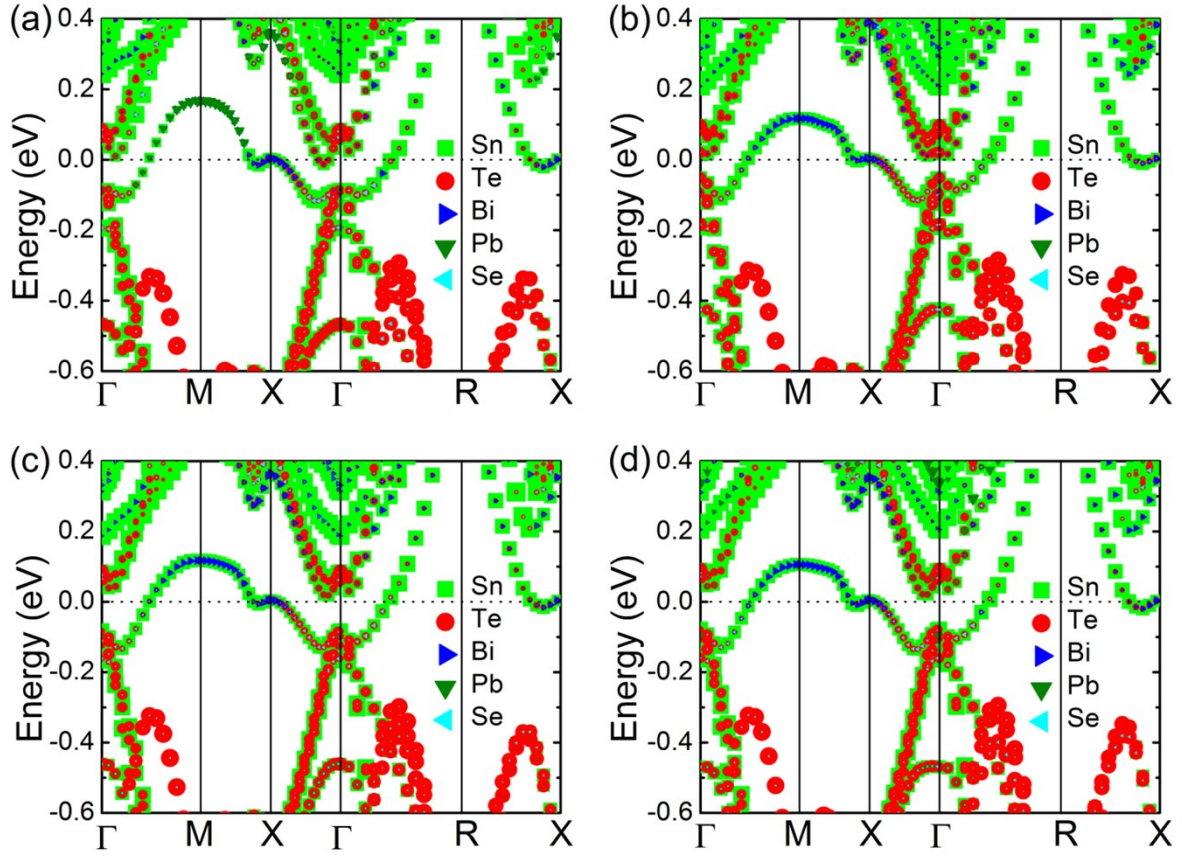


Figure S15. The projected band structures with different pair distances of Bi-Pb and Bi-Se in $\text{Sn}_{0.97}\text{Bi}_{0.03}\text{Te}-3\% \text{PbSe}$: Bi-Pb and Bi-Se are in the (a) nearest neighbour (NN) sites; (b) second nearest neighbour site (2NN); (c) third nearest neighbor (3NN) sites; (d) fourth nearest neighbor NN sites. The energies are shifted with respect to the Fermi energy, which is set to zero. The different configurations of defects have same electronic band structure.

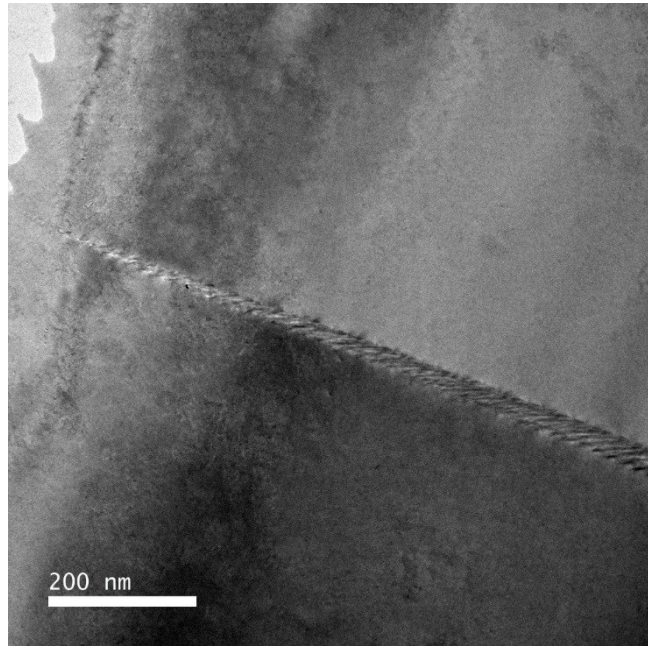


Figure S16. TEM image of grain boundary along [111] zone axis.

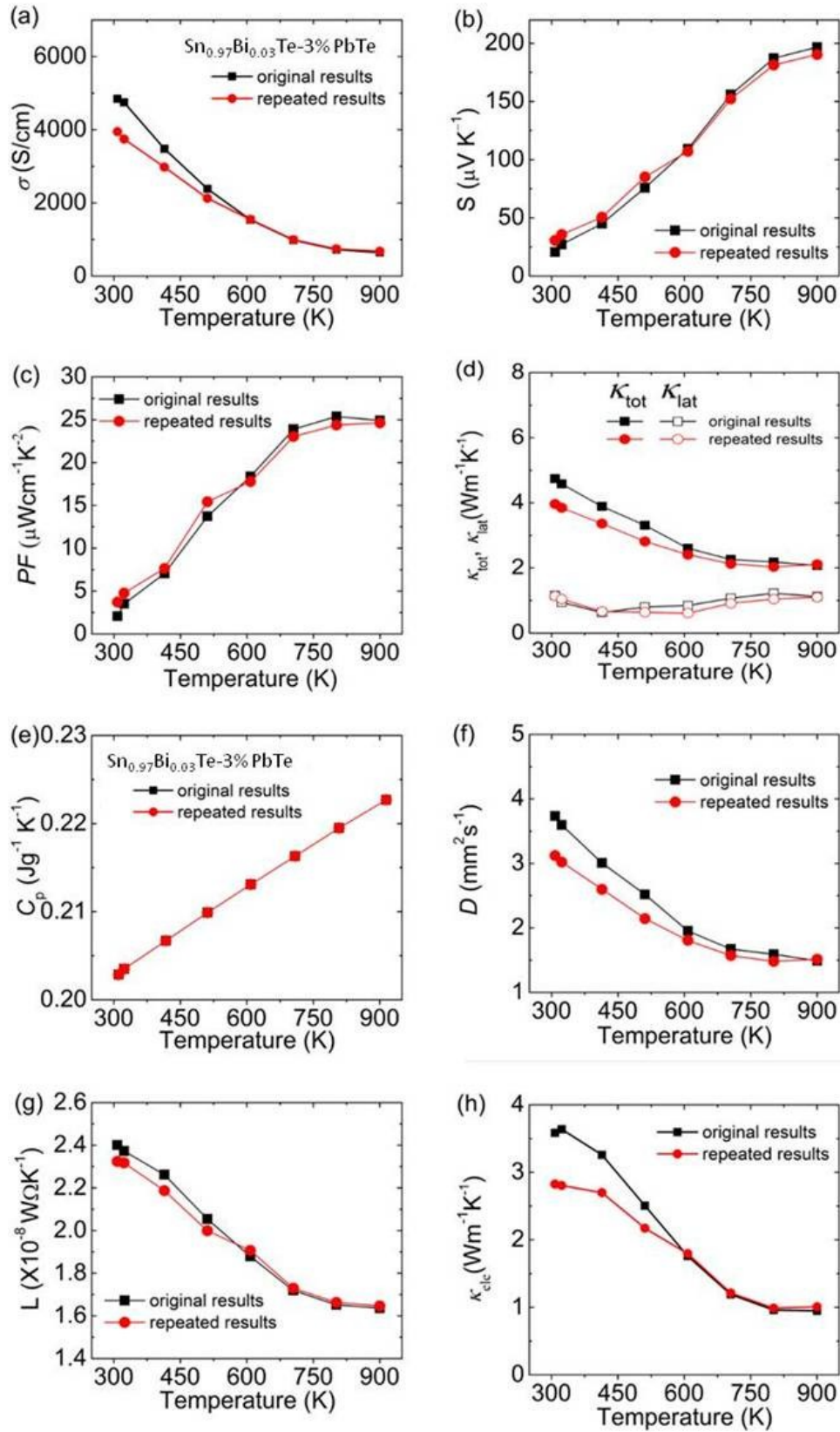


Figure S17. The original and repeated experimental results for $\text{Sn}_{0.97}\text{Bi}_{0.03}\text{Te}-3\% \text{PbTe}$: (a) electrical conductivity; (b) Seebeck coefficient; (c) power factor; (d) total and lattice thermal conductivities; (e) heat capacity; (b) thermal diffusivity; (c) Lorenz number; (d) electronic thermal conductivity.

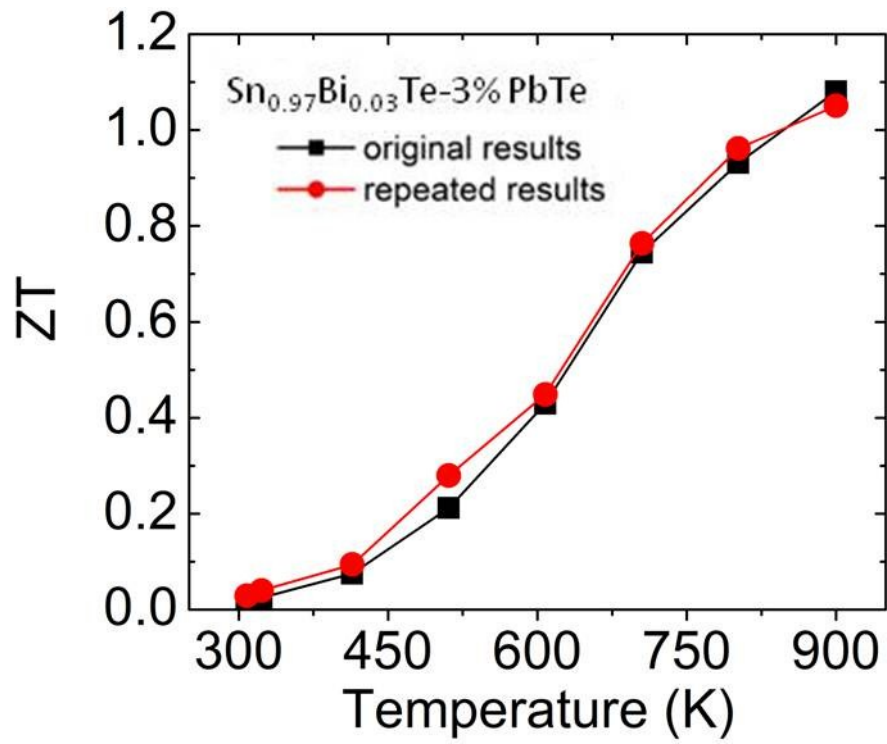


Figure S18. ZT values of original and repeated experimental results for $\text{Sn}_{0.97}\text{Bi}_{0.03}\text{Te}-3\%$ PbTe.